

Precision Nanocluster-Based Toroidal and Supertoroidal Frameworks Using Photocycloaddition-Assisted Dynamic Covalent Chemistry

Kavalloor Murali Lakshmi, Jose V. Rival, Pakath Sreeraj, Sindhu R. Nambiar, Chinnaiah Jeyabharathi, Nonappa, and Edakkattuparambil Sidharth Shibu*

Dedicated to Professor Thalappil Pradeep on the occasion of his 60th Birthday

Atomically precise nanoclusters (NCs) have recently emerged as ideal building blocks for constructing self-assembled multifunctional superstructures. The existing structures are based on various non-covalent interactions of the ligands on the NC surface, resulting in inter-NC interactions. Despite recent demonstrations on light-induced reversible self-assembly, long-range reversible self-assembly based on dynamic covalent chemistry on the NC surface has yet to be investigated. Here, it is shown that Au₂₅ NCs containing thiolated umbelliferone (7-hydroxycoumarin) ligands allow [2+2] photocycloaddition reaction-induced self-assembly into colloidal-level toroids. The toroids upon further irradiation undergo inter-toroidal reaction resulting in macroscopic supertoroidal honeycomb frameworks. Systematic investigation using electron microscopy, atomic force microscopy (AFM), and electron tomography (ET) suggest that the NCs initially form spherical aggregates. The spherical structures further undergo fusion resulting in toroid formation. Finally, the toroids fuse into macroscopic honeycomb frameworks. As a proof-of-concept, a cross-photocycloaddition reaction between coumarin-tethered NCs and an anticancer drug (5-fluorouracil) is demonstrated as a model photo-controlled drug release system. The model system allows systematic loading and unloading of the drug during the assembly and disassembly under two different wavelengths. The results suggest that the dynamic covalent chemistry on the NC surface offers a facile route for hierarchical multifunctional frameworks and photocontrolled drug release.

materials.^[1] Their unique size and shape-dependent properties and functional surface ligands allow self-assembly under a variety of environmental settings and stimuli. Different non-covalent nanoscale surface forces and hydrophobic effects have been used to control inter-NP interactions leading to thermodynamically stable equilibrium structures.^[1a,b] Recent demonstrations have also suggested that plasmonic NPs with light-responsive ligands allow out-of-equilibrium systems and dynamic self-assembly.^[2] These supramolecular organizations may open up new possibilities for a variety of applications, including optoelectronic device manufacturing, antibiotic detection, chiral plasmonics, catalysis, and bioimaging.^[3] However, achieving monodispersity with plasmonic NPs is a challenging task. Moreover, large NPs have strong aggregation tendencies and uncontrolled surface ligand density. Therefore, well-defined long-range order with reproducible properties is a challenge. Recent reports have also suggested that polydisperse NPs and strictly monodisperse NPs display different self-assembly behavior.^[4] In this

1. Introduction

The self-assembly of noble metal nanoparticles (NPs) has emerged as an important route for advanced multifunctional


context, precision NCs holding well-defined structures, strictly monodisperse nature, thermodynamic stability, and thermal and photostability are ideal building blocks for controlled structure formation across-length scales.^[5] Surface engineering

K. M. Lakshmi, C. Jeyabharathi
Electroplating and Metal Finishing Division (EMFD)
Council of Scientific and Industrial Research (CSIR)-Central
Electrochemical Research Institute (CECRI)
Karaikudi, Tamil Nadu 630003, India

K. M. Lakshmi, S. R. Nambiar, C. Jeyabharathi
Academy of Scientific and Innovative Research (AcSIR)
Ghaziabad 201002, India

J. V. Rival, P. Sreeraj, E. S. Shibu
Smart Materials Lab (SML)
Department of Nanoscience and Technology (DNST)
University of Calicut (UoC)
Malappuram, Kerala 673635, India
E-mail: shibu@uoc.ac.in

S. R. Nambiar
Food Safety and Analytical Quality Control Laboratory
CSIR-Central Food Technological Research Institute (CFTRI)
Mysuru, Karnataka 570020, India
Nonappa
Faculty of Engineering and Natural Sciences
Tampere University
Tampere FI 33720, Finland

 The ORCID identification number(s) for the author(s) of this article can be found under <https://doi.org/10.1002/smll.202207119>.

DOI: 10.1002/smll.202207119

of NCs with functional ligands allows self-assembly by utilizing attractive nanoscale driving factors.^[6] These directional forces have the potential to arrange NCs into supramolecular superstructures including 2D crystals,^[7] colloidal capsids,^[7] frameworks,^[8] and macroscopic elastic membranes.^[9] Such structures have potential applications in gas sensing or storage,^[10] green catalysis,^[11] light-emitting devices,^[12] and theranostics.^[13] NC self-assembly has also been demonstrated using light-responsive surface ligands. For example, photo-responsive reversible self-assembly in Au₂₅ NCs tethered with azobenzene or spiropyran molecules is well known in this area.^[14] Though the [2+2] cycloaddition reaction of chromophores (e.g., coumarin moieties) connected to the surface of gold NPs has been demonstrated,^[15] analog reactions on the NC surface have yet to be achieved. Long-range self-assembly of NCs based on such photocycloaddition reaction is still in its infancy due to the difficulties in synthesizing thiolated chromophore-tethered monodisperse NCs. NCs covalently linked to chromophores capable of undergoing [2+2] photocycloaddition will provide photosensitive reaction sites for light-induced dimerization and subsequent assembly.

In this work, we show the synthesis and light-mediated assembly of coumarin thiol-stapled Au₂₅ NCs, [Au₂₅(C₉-CMT)₁₈]⁻. Illumination of NCs dispersed in tetrahydrofuran (THF) at 365 nm resulted in uniform toroidal superstructures facilitated by inter-NC coupling via cycloaddition reaction. Using extensive spectroscopic studies and microscopic imaging we show that initially formed transient spherical structures undergo fusion and transformations into toroids. Sustained irradiation of light results in inter-toroidal coupling facilitated by the cycloaddition at the supercolloidal-level resulting in macroscopic honeycomb structures. Beyond hierarchical structure formation, we also demonstrate intermolecular photocycloaddition reaction between coumarin-tethered NCs and 5-fluorouracil (5-FU, an anticancer drug) towards a model photocontrolled drug delivery system. The drug-loaded superstructures fragmented into individual NCs and drug molecules when exposed to 254 nm light, demonstrating their photoreversibility. These NCs with improved photostability and photosensitive functional ligands are anticipated to offer new routes for combined theranostics and advanced drug delivery.

2. Results and Discussion

2.1. Synthesis and Characterization of [Au₂₅(C₉-CMT)₁₈]⁻ NCs

We first discuss the synthesis and characterization of Au₂₅ NCs capped with various ligands. Initially, we investigated the thermodynamic feasibility of Au₂₅ NC formation by altering the spacer length of the chromophore. Only chromophores with suitable molecular spacing meet the solubility threshold, resulting in NC formation. To test this, we connected 7-hydroxycoumarin (umbelliferone) moieties with short-chain (C₃) and long-chain (C₉) thiols (Figure 1a). The detailed protocols for the synthesis and characterization of coumarin-alkyl monothiols (C₃-CMT and C₉-CMT) are provided in the experimental section (Figures S1–S15, Supporting Information). The synthesis of C₃-CMT- and C₉-CMT-tethered Au₂₅ NCs were carried out using a modified

Brust-Schiffrin single-phase approach.^[16] Spectroscopic results suggest that Au₂₅ NCs are produced exclusively with C₉ spacers (Figure 1b). The detailed procedure for the synthesis and purification of [Au₂₅(C₉-CMT)₁₈]⁻ NCs is provided in the experimental section. The energy-minimized structure of [Au₂₅(C₉-CMT)₁₈]⁻ NC using density functional theory (DFT) is provided in Figure 1b. The evolution of NCs is verified by comparing the UV–vis absorption spectra of C₉-CMT and [Au₂₅(C₉-CMT)₁₈]⁻ NCs dispersed in THF with well-established [Au₂₅(PET)₁₈]⁻ NC (Figure 1c). Au₂₅ NCs show a characteristic absorption band ca. 680 nm due to the HOMO-LUMO electronic transitions. Two additional peaks ca. 440 and 395 nm represent the HOMO-sp and d-sp transitions, respectively. The prominent peak ca. 320 nm in the absorption spectra is due to the π - π^* transition in coumarin moiety. Inset in Figure 1c shows an expanded region of UV–vis absorption spectra illustrating the unique features of Au₂₅ NCs. The core size, purity, and molecular composition of NCs were characterized using matrix-assisted laser desorption/ionization time-of-flight (MALDI-TOF) mass spectrometry (Figure 1d). The computed mass of [Au₂₅(C₉-CMT)₁₈]⁻ NCs matches well with the molecular ion peak ca. 10674 Da, confirming the precision in the molecular composition (inset in Figure 1d). The two additional peaks ca. 8612 and 8044 Da in the full spectrum refer to the loss of Au_n(C₉-CMT)_n (n = 4 and 5) fragments during ionization.^[17a] The presence of coumarin moieties on the NC surface was verified by comparing the proton nuclear magnetic resonance (¹H NMR) spectra of [Au₂₅(C₉-CMT)₁₈]⁻ NCs with that of C₉-CMT in chloroform-d (CDCl₃) and THF-d₈ (Figure S16, Supporting Information). While the ¹H resonance peaks of pure ligands appeared sharp, in the case of NCs, they turned broad presumably due to the large size and overlapping of signals from chemically and magnetically non-equivalent ligands on the NC surface.^[17b] Significant changes were observed in ¹H NMR signal of the methylene group linked to the thiol (-CH₂SH) moiety. In the case of pure ligand, the ¹H NMR signal of -CH₂SH appeared at 2.51 ppm. However, in NCs we observed a downfield shift to 3.28 ppm (CDCl₃) owing to deshielding from the metal core. The change in the multiplicity of the methylene group close to sulfur from quartet to broad triplet represents the development of an Au–S bond by deprotonating the -SH group. The absence of -SH stretching band ca. 2543 cm⁻¹ in Fourier transform infrared (FT-IR) spectra of [Au₂₅(C₉-CMT)₁₈]⁻ NCs also support covalently linked thiols (Figure S17, Supporting Information). The X-ray photoelectron spectroscopy (XPS) analysis from [Au₂₅(C₉-CMT)₁₈]⁻ NCs revealed the binding energies (BE) of Au 4f_{7/2} and Au 4f_{5/2} at 83.92 and 87.62 eV (Figure 1e). The results agree well with the BE values of [Au₂₅(PET)₁₈]⁻ NCs (84.39 and 88.01 eV, Figure 1f). The variation in the electron density of bound ligands may cause a small change in the BE values of these NCs. The BE values of S 2p (Figure 1g,h), C 1s, and O 1s levels (Figure S18, Supporting Information) of [Au₂₅(C₉-CMT)₁₈]⁻ and [Au₂₅(PET)₁₈]⁻ NCs are also provided. Transmission electron microscopy (TEM) images of [Au₂₅(C₉-CMT)₁₈]⁻ NCs show a narrow size distribution (1.3 ± 0.2 nm; Figure 2c). The histogram from the TEM micrograph (inset in Figure 2c) is consistent with the reported values for such NCs.^[18] A slight broadening in the size distribution of NCs presumably arises due to their instability under high-energy electron beams.

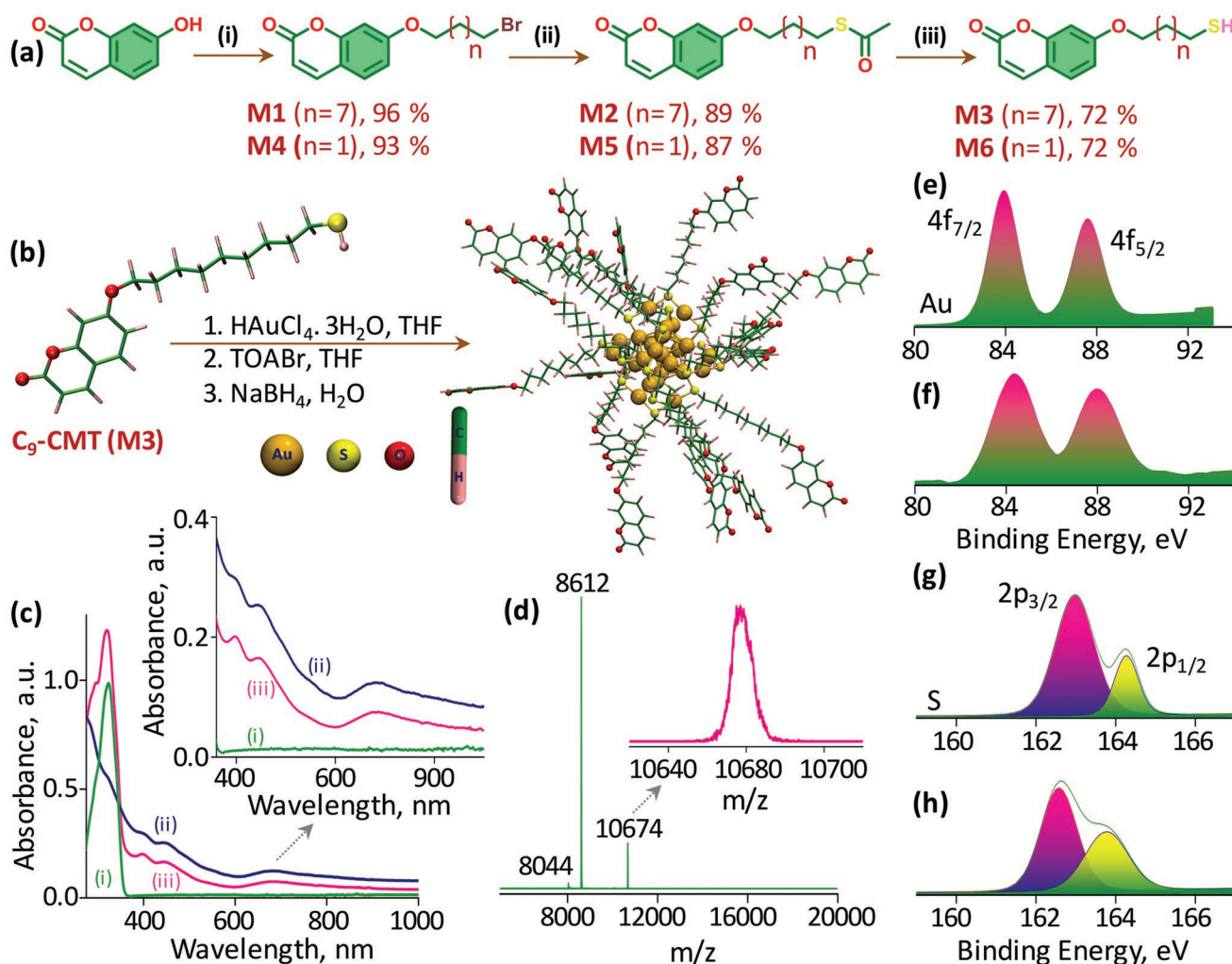


Figure 1. Synthesis and characterization of NCs. a) Scheme for the synthesis of C₉-CMT (M3) or C₃-CMT (M6); i) 1,9-dibromononane or 1,3-dibromopropane, K₂CO₃, KI, acetone, reflux, 4 h; ii) KSCoCH₃, acetone, RT, overnight; iii) 1.25 M HCl/CH₃OH, reflux, 2 h. The chemical reaction yields of M1–M6 are given. b) Schematic shows the synthesis of [Au₂₅(C₉-CMT)₁₈]⁻ NCs and their energy-minimized structure. c) UV-vis absorption spectra of i) C₉-CMT, ii) [Au₂₅(PET)₁₈]⁻, and iii) [Au₂₅(C₉-CMT)₁₈]⁻ NCs. An enlarged view of UV-vis absorption spectra is shown in the inset. The MALDI-TOF mass spectrum recorded from [Au₂₅(C₉-CMT)₁₈]⁻ NCs is shown in (d) An enlarged view of the molecular ion peak is given in the inset. The XPS spectra recorded from e,g) [Au₂₅(C₉-CMT)₁₈]⁻ and f,h) [Au₂₅(PET)₁₈]⁻ NCs show the presence of (e and f) Au 4f levels and (g and h) S 2p levels.

2.2. Photocycloaddition and Toroid Formation

The light-induced [2+2] cycloaddition is an established reaction in photochemistry for producing dimers. For instance, the coumarin can undergo cyclodimerization at the 3,4-double bond of the pyrone ring under 365 nm illumination. This will result in the formation of cyclobutane adducts by linking two strong sigma bonds between the chromophores (Figure 2b). We first studied the photodimerization ability of ligand (C₉-CMT) using time-dependent absorption spectra recorded after 365 nm illumination. The temporal UV-vis absorption spectra measured from C₉-CMT dispersed in THF and illuminated under 365 nm light are shown in Figure S19, Supporting Information. When exposed to light, C₉-CMT absorption spectra show a progressive drop in optical density (OD) around 320 nm. This suggests the photodimerization of the coumarin molecules.^[19] Before performing the photodimerization process, [Au₂₅(C₉-CMT)₁₈]⁻

NC was further purified using preparative thin-layer chromatography (PTLC). We carried out the photodimerization of [Au₂₅(C₉-CMT)₁₈]⁻ NCs by irradiating a solution of NCs in THF (≈ 0.01 mM) under 365 nm light. Figure 2a represents the temporal UV-vis absorption spectra recorded from NC solution illuminated continuously for up to 8 h at room temperature (25 °C). To reduce temperature fluctuations and solvent loss throughout the photodimerization process, we kept the NC solution within a closed container in an ice bath under dark conditions. The optical absorption spectra collected from the NC solution followed the same pattern as C₉-CMT. This indicates that the photocycloaddition reaction between the surface ligands bound to adjacent NCs was successful. Even though NCs produced dimers via photochemical reaction, they were able to preserve their unique optical absorption features (Inset a₁ in Figure 2). The intrinsic optical features of NCs (680 nm) sustained after extended exposure indicate their better

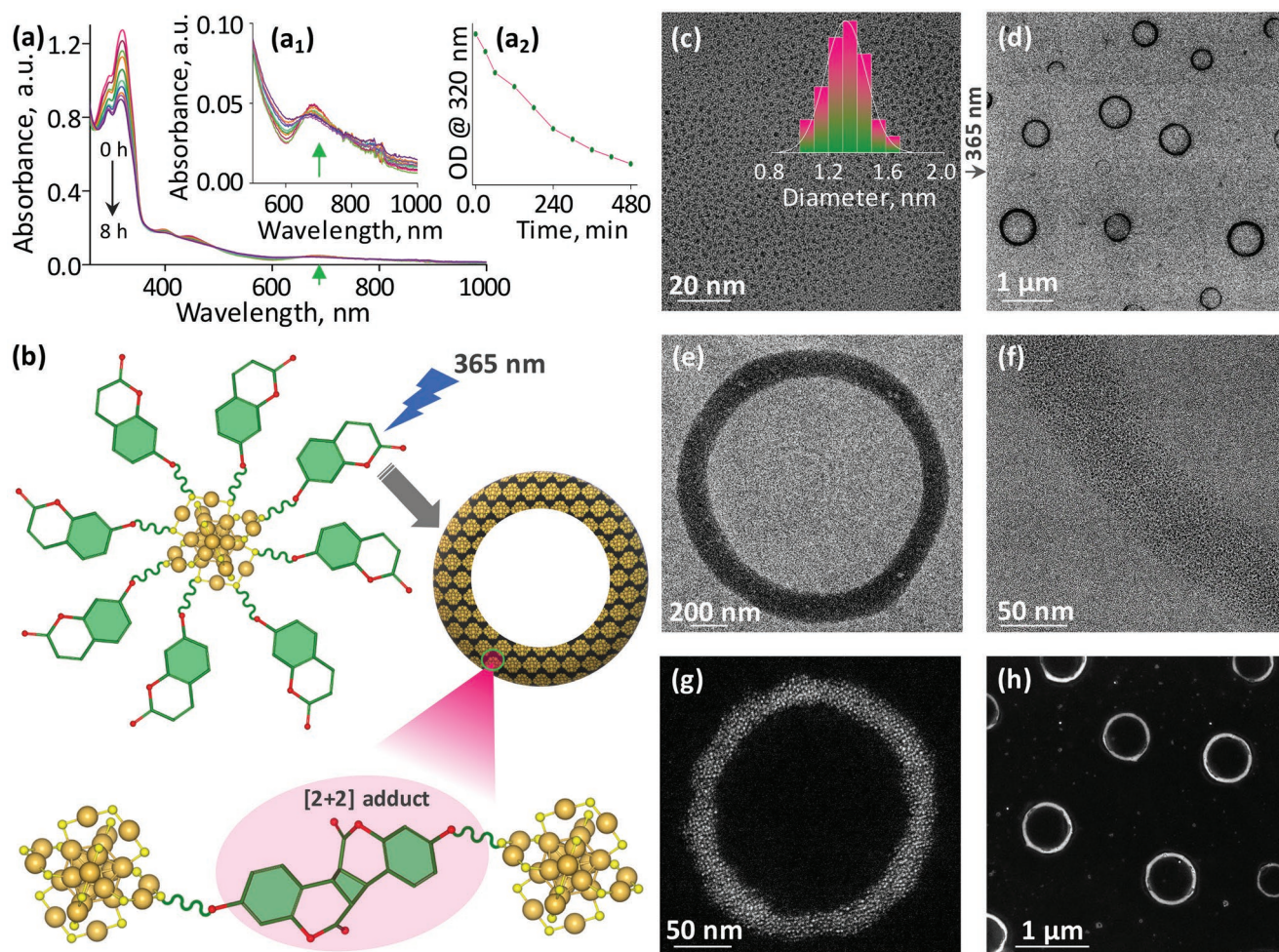


Figure 2. Photodimerization and self-assembly of NCs. a) Temporal UV–vis absorption spectra of $[\text{Au}_{25}(\text{C}_9\text{-CMT})_{18}]^-$ NCs recorded under 365 nm illumination. Insets a_1 and a_2 show an enlarged view of the HOMO-LUMO band as well as changes in OD as a function of illumination time. b) A schematic showing the photodimerization and self-assembly of $[\text{Au}_{25}(\text{C}_9\text{-CMT})_{18}]^-$ NCs. c, d) TEM micrographs of $[\text{Au}_{25}(\text{C}_9\text{-CMT})_{18}]^-$ NCs c) before, and d) after 365 nm lighting. e, f) Zoomed-in and focused HRTEM micrographs of e) a single toroid, and f) the edge of a toroid. g, h) STEM images of g) a magnified view of a single toroid, and h) large area toroidal self-assembly.

photostability. A plot of OD (ca. 320 nm) versus irradiation time is shown in inset a_2 in Figure 2. We further investigated the photodimerization of NCs using TEM and scanning transmission electron microscopy (STEM) imaging. Remarkably, long-term illumination of $[\text{Au}_{25}(\text{C}_9\text{-CMT})_{18}]^-$ NCs resulted in the formation of the uniform toroidal assembly via photodimerization (Figure 2d). The high-magnification TEM images of a single toroid with well-organized individual NCs on the toroidal rim confirm the self-assembly (Figure 2e, f). The above observations suggest that the [2+2] cycloaddition of bound ligands on the nearby NCs promotes inter-NC bonding and the development of colloidal-level toroids as shown schematically in Figure 2b. The cycloaddition chemistry between nearby coumarin molecules tethered on the NC surface is evident from the ^1H NMR spectrum of the toroidal solution in THF-d_8 (Figure S20, Supporting Information). A partial disappearance of the photoactive double bond protons of coumarin (peak a at 7.69 ppm and peak b at 6.11 ppm) and the appearance of cyclobutane protons (peak a_1 at 3.82 ppm and b_1 at 4.33 ppm)^[19c] further confirmed

the formation of toroids via photodimerization. The presence of both types of protons in the NMR spectrum shows that only a few coumarin molecules underwent the [2+2] cycloaddition reaction. The better colloidal stability of toroids is presumably due to such controlled photo-crosslinking reactions between NCs. One could assemble NCs at larger concentrations using a high-power light source. However, NCs were decomposed when illuminated under a high-power light source (Figure S21, Supporting Information). Figure 2h shows a large area STEM image of the toroidal assembly, whereas Figure 2g provides a higher magnification view of a single toroid showing individual NCs. The energy-dispersive X-ray analysis (EDS) supports the presence of Au, S, O, and C in assembled NCs. The elemental mapping (gold and sulfur) and corresponding spectrum from the toroid are shown in Figure S22, Supporting Information. To ensure toroidal formation in solution, dynamic light scattering (DLS) measurements were performed (Figure S23, Supporting Information). During the illumination of NC solution under 365 nm, the average particle size was increased to ≈ 60 nm

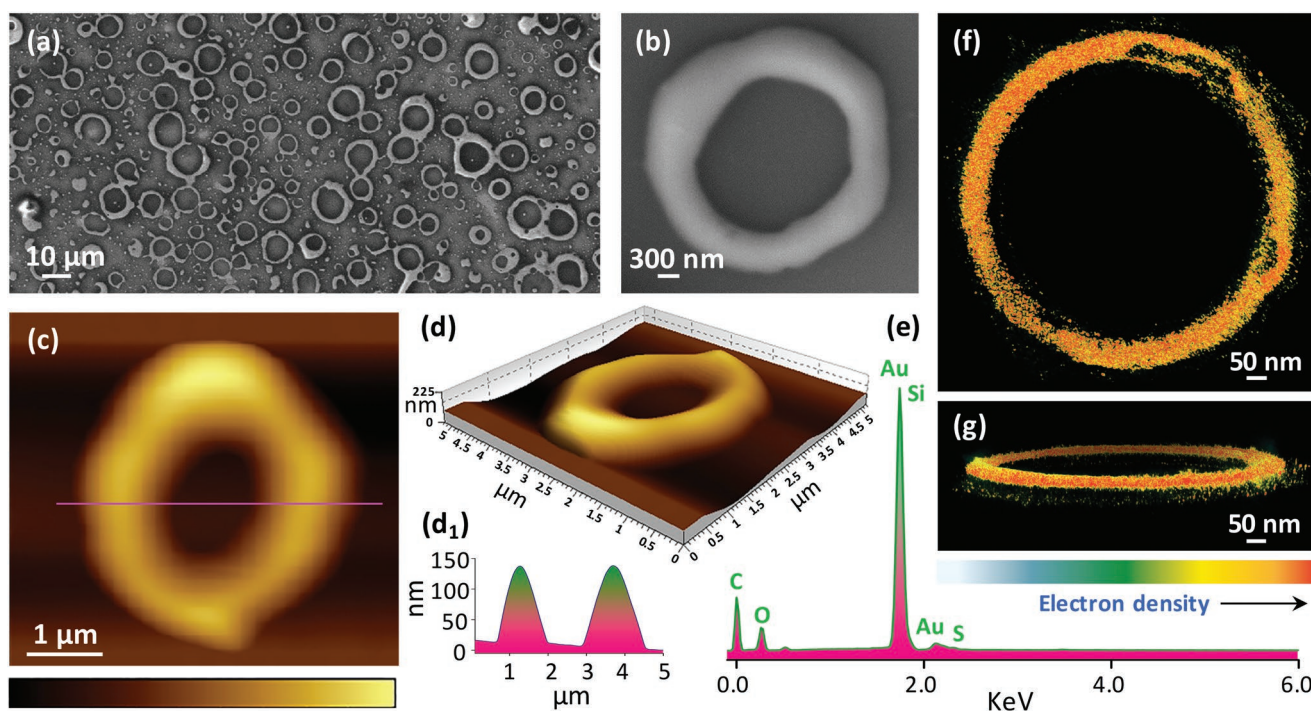


Figure 3. Morphology of toroids. a) Larger area FESEM image of self-assembled toroids and b) zoomed-in and focused image of a single toroid. c,d) AFM images c) topography, d) amplitude and corresponding (d₁) height profile of a single toroid captured after 8 h of illumination. e) Elemental spectrum collected from the toroid. f,g) 3D reconstructed tomograms of a toroid shown in different orientations.

(2 h), then to ≈ 100 nm (4 h), and finally to ≈ 130 nm (6 h). The gradual increment in the particle size showed the formation of toroids (the thickness of the toroidal rim increased). To understand the stability of toroids in dark, we recorded and examined the absorption spectra of the assembled solution stored in dark (Figure S24, Supporting Information). The toroids showed unaltered optical absorption features indicating their excellent stability in the dark. TEM images (Figure S25, Supporting Information) from the assembled superstructures stored in the refrigerator (more than a year) also showed uniform toroids, demonstrating the long-term stability of the toroidal assembly.

The morphology of the self-assembled toroids was further investigated using field emission scanning electron microscopy (FESEM) and AFM imaging (Figure 3). Larger area FESEM images of the photodimerized NCs showed assembled toroids distributed all over the substrate (Figure 3a). Figure 3b shows the FESEM image of a single toroid with an outer diameter of ≈ 3 μm . The elemental composition analysis of assembled toroids using EDS revealed the presence of carbon, oxygen, gold, and sulfur (Figure 3e). Corresponding elemental maps of gold and sulfur are shown in Figure S26, Supporting Information. AFM topography image (tapping mode) of an individual toroid with an average outer diameter of ≈ 4 μm and a rim diameter of ≈ 1.6 μm is shown in Figure 3c. From the 3D view (amplitude) of the assembled toroid (Figure 3d) and corresponding height profile (Figure 3d₁), the average thickness of the toroid is found to be ≈ 140 nm. A wide area AFM micrograph of toroidal assembly is provided in Figure S27, Supporting Information. Since the morphology of assembled NCs in AFM, FESEM, and TEM is similar, one can easily exclude the electron beam-assisted assembly of

NCs. To gain further insights into 3D structural details, transmission ET reconstruction was performed for toroidal structures. Figure S28, Supporting Information, displays TEM micrographs of the toroidal assembly at different tilt angles (-53 , 0 , and $+53$ degrees). The 3D reconstruction and cross-sectional views show a toroidal rim with uniform thickness and diameter (Video S1, Supporting Information, and Figure 3f,g). The toroidal structures are comprised of multilayered and densely packed NCs. The ET reconstruction data are consistent with the AFM data.

2.3. Mechanism for the Toroidal Formation

Due to the unique structure and applications of toroids, several approaches including direct assembly,^[20] morphological transition,^[21] and hierarchical system reconstruction^[22] have been used to construct them from organic molecules, polymers, and other building blocks.^[23] However, toroidal superstructures using NC self-assembly have not been reported in the literature. To better understand the mechanism of toroidal formation, FESEM and AFM imaging of NCs under 365 nm illumination were performed every 1.5 h interval. Figure 4a–d shows the FESEM images from the NC solution (≈ 0.01 mM in THF) after 1.5, 3, 4.5, and 6 h of illumination at 365 nm. Surprisingly, the FESEM micrograph (Figure 4a) shows that NCs were initially assembled into spherical structures (100–500 nm size). After another 1.5 h of irradiation, these spherical superstructures tend to combine (Figure 4b). Over the course of 4.5 h, spheres were transformed into premature toroids (Figure 4c). After 6 h of illumination, well-defined micron-sized toroids were formed

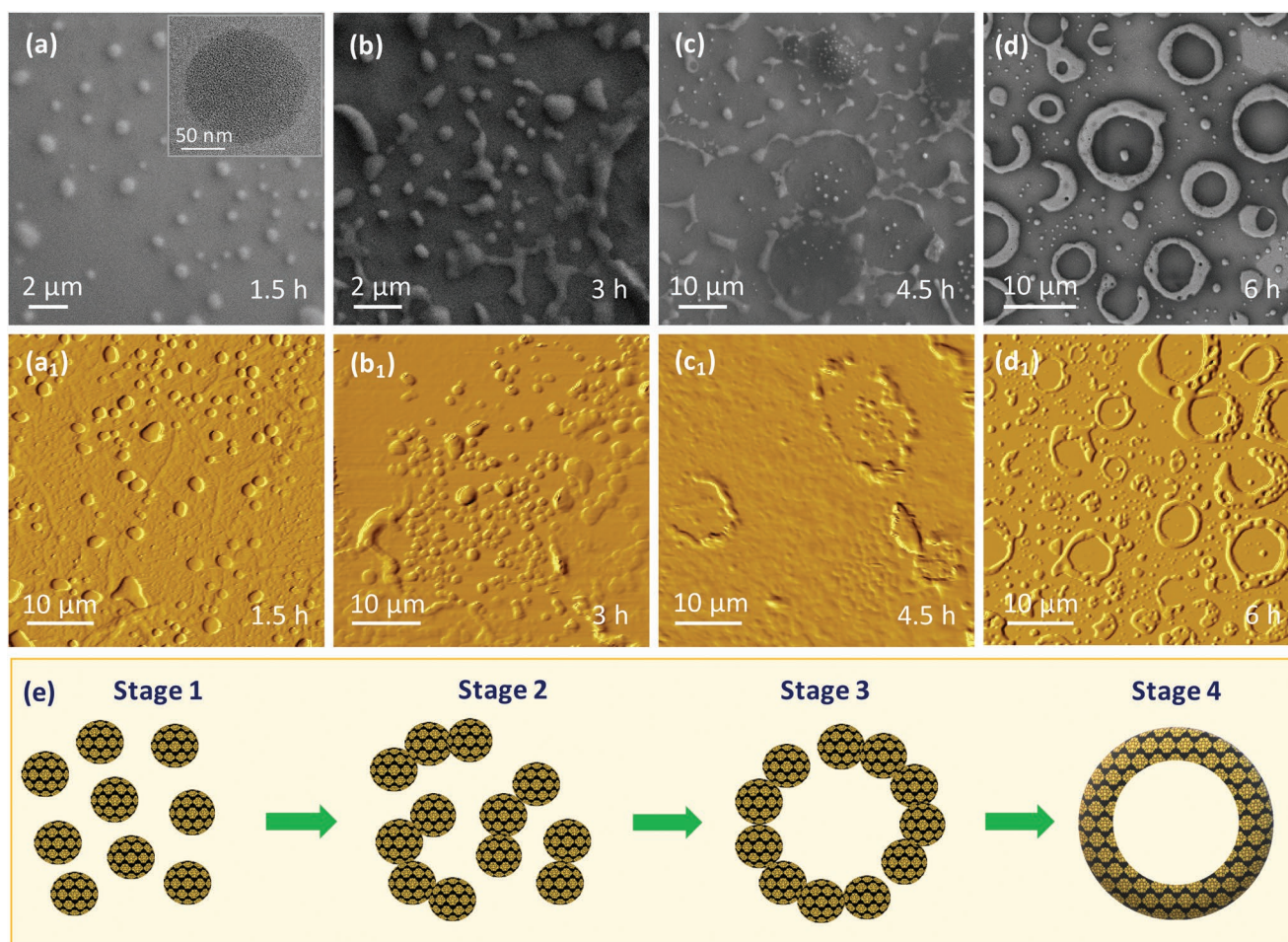


Figure 4. The mechanism for the toroidal formation. a–d) Temporal FESEM images of $[\text{Au}_{25}(\text{C}_9\text{-CMT})_{18}]^-$ NC solution after 365 nm irradiation for a) 90, b) 180, c) 270, and d) 360 min. Figure (a₁–d₁) depicts the corresponding AFM images. The inset of (a) shows the TEM micrograph of a single assembled sphere. Scheme (e) depicts the various stages of toroidal formation.

(Figure 4d). Scheme 4e shows different stages of toroidal formation and corresponding AFM images are given in Figure 4a₁–d₁. The initial stage of the assembly facilitates the reorganization of spheres into more energy-minimized toroids (morphological transition).^[21] The heterogeneity in the size of the resulting toroids could be explained by the uncontrolled assembly of polydisperse spheres. The formation of spheres at the beginning of the irradiation confirms that the above-described toroid development is not driven by simple evaporation.

2.4. Macroscopic Supertoroidal Honeycomb Frameworks

The consequence of long-term irradiation on toroidal structural rearrangement was systematically investigated. For this, the NC solution prepared in THF was exposed to UV light (365 nm) for 32 h. Interestingly, the prolonged irradiation of NCs resulted in macroscopic honeycomb superstructures via inter-toroidal coupling (Figure 5a). High-resolution TEM imaging of the frameworks reveals that they are composed of assembled NCs, as shown in Figure 5b,c. Notably, the characteristic optical absorption features and size of the NCs were preserved even after the

formation of porous frameworks. The morphology of such fused toroidal superstructures was further confirmed by recording and analyzing the FESEM images. Figure 5d shows a large area FESEM image of porous frameworks formed during the sustained illumination of NCs at 365 nm. The morphology and thickness of fused toroids were further examined using AFM. Figure 5e,f shows the AFM (topography) and corresponding height profile of the honeycomb framework, respectively. Under prolonged lighting, the average thickness of the assembled superstructures increased from ≈ 140 nm (Figure 3d₁) to ≈ 1 μm . This indicates that photocycloaddition is occurring in the XY and Z planes during inter-toroidal coupling. A schematic of such a coupling reaction is shown in Figure 5g.

2.5. Phototriggered Drug Conjugation and Release

Finally, the ability of $[\text{Au}_{25}(\text{C}_9\text{-CMT})_{18}]^-$ NCs to host and transport drug molecules has been investigated by exploiting their photosensitive double bonds. As a model system, we used a well-known anticancer drug 5-fluorouracil (5-FU), which has a photoactive double bond. To demonstrate the efficiency of

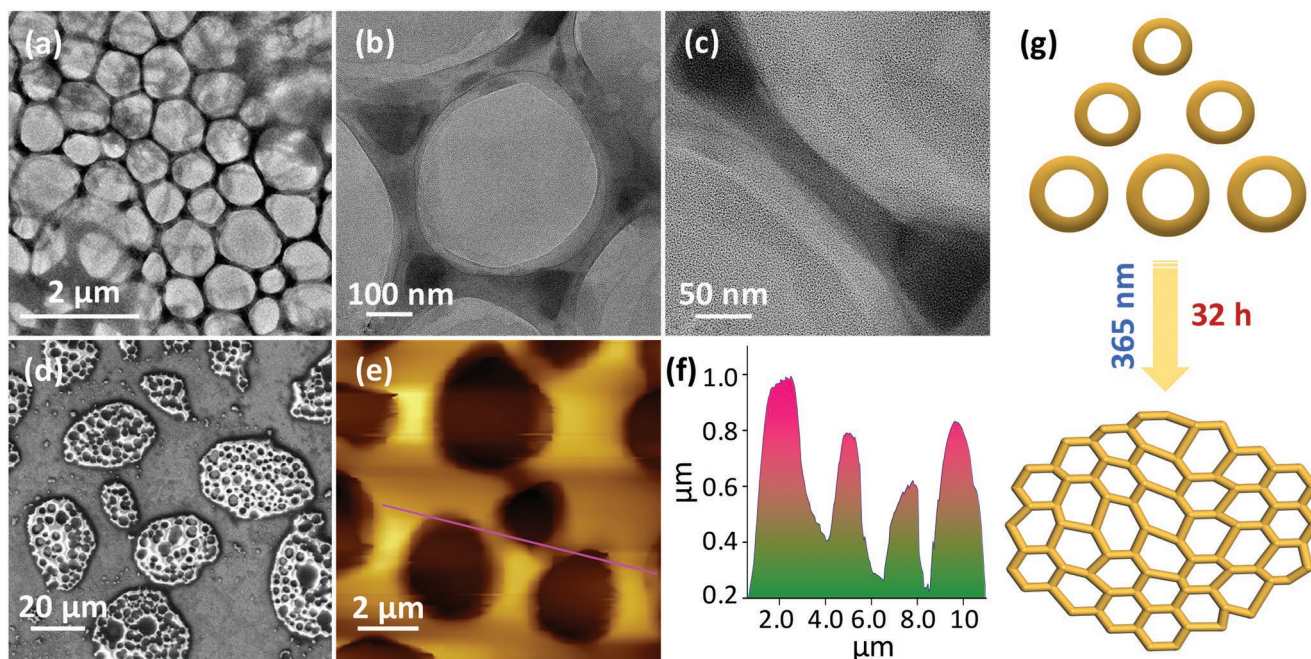


Figure 5. The effect of continuous lighting on the structural rearrangement of toroids. a) Large area TEM image of assembled NCs after 32 h of illumination. b,c) Zoom-in and focused TEM images of b) a single fused toroidal ring and c) its edge. d) Larger area FESEM image of honeycomb superstructures. e) AFM topography image and f) height profile of the porous framework. Scheme (g) depicts the inter-toroidal coupling.

the proposed light-triggered drug delivery system, $[\text{Au}_{25}(\text{C}_9\text{-CMT})_{18}]^-$ NC solution in THF (≈ 0.01 mM) was mixed with 20 equivalents of 5-FU (100 μL *N,N'*-dimethylformamide; DMF). The mixture was then continuously stirred at 24 °C for 8 h while being exposed to continuous 365 nm radiation. The UV-vis absorption spectra of the solution showed a systematic decrease in OD around 320 nm (Figure S29, Supporting Information), which was consistent with the data shown in Figure 2a. The drug-loaded NC conjugate (NC-FU) was purified by precipitating the reaction mixture with excess methanol and multiple (three times) washing with methanol. TEM and STEM imaging of the purified NC-FU conjugate showed the formation of spherical NC assemblies (Figure 6b-e). Notably, similar assembled spheres were the first set of intermediates formed in the case of pure $[\text{Au}_{25}(\text{C}_9\text{-CMT})_{18}]^-$ NCs immediately after 1.5 h illumination (Figure 4a). Aside from the classic cycloaddition reaction between coumarin moieties tethered on adjacent NCs, cross-photocycloaddition between bound coumarins and 5-FU is also possible. As a result, there will be a limited number of photoactive coumarin moieties on the NC surface, which will eventually slow down NC assembly in the presence of excess 5-FU (8 h). In addition, the bound 5-FU on the NC surface hinders the rearrangement of spheres into toroids, hence the extended irradiation resulted in no toroidal structures. A schematic representation for the formation of spherical assembly from NC-FU conjugate is shown in Figure 6a. The presence of gold, sulfur, fluorine, and nitrogen under STEM and FESEM EDS shows 5-FU in the assembly (Figure 6f and Figure S30, Supporting Information). Since two types of photoreactions occurred on the surface of NCs at the same time, the ^1H NMR spectrum was complex to investigate the drug loading in detail (Figure S31, Supporting

Information). However, the presence of three additional signals at 5.53 (g_1), 4.71 (b_2), and 4.63 ppm (a_2) in addition to the cyclobutane protons from coumarin dimers (Figure S20, Supporting Information) at 3.82 (a_1) and 4.33 ppm (b_1) suggests the covalent loading of drug molecules via cyclobutane linkage. The efficiency of the cross-photocycloaddition reaction is found to be relatively lower compared to NC alone assembly, which is in good agreement with TEM data (Figure 6b-e). The limited drug loading could be probably due to the competition between homo- and cross-photocycloaddition reactions between coumarin and 5-FU. The average thickness of the NC-FU spherical assembly measured from the AFM height profile (Figure S32, Supporting Information) shows ≈ 90 nm, which is less than the average thickness of the toroid (≈ 140 nm) shown in Figure 3d₁. This suggests that the cross-photocycloaddition reaction limits not only toroidal formation but also assembled growth along the Z axis. The ET reconstruction of the NC-FU assembly (Figure 6g-i and Video S2, Supporting Information) revealed that the superstructure is disc-like or a deformed sphere. The cross-sectional images show that the assembled structures comprise thickly packed NCs. The data shown above are in accord with the TEM, STEM, and AFM micrographs shown in Figure 6d,e and Figure S32, Supporting Information, respectively. The presence of nitrogen and fluorine in the NC-FU assembly was further confirmed in the XPS analysis (Figure S33, Supporting Information). Importantly, when a solution of NC-FU assembly was exposed to 254 nm light, a gradual change in the optical absorption features was observed (Figure S34a, Supporting Information). This indicates the light-induced release of drug molecules from the NC-FU conjugate by cleaving the cyclobutane adduct. Such photocaging could eventually disassemble the NCs into individual

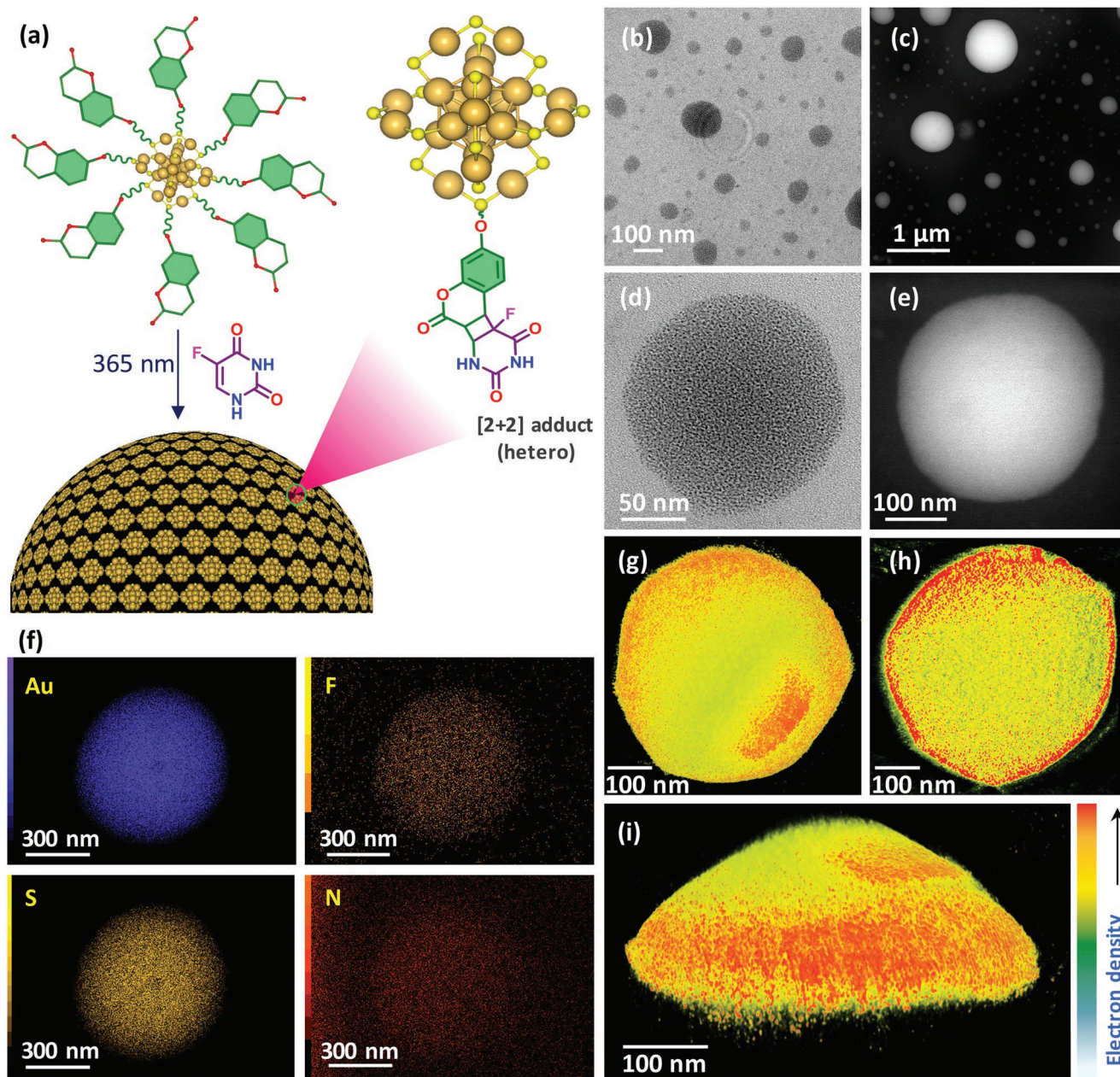


Figure 6. [Au₂₅(C₉-CMT)₁₈]⁻ NCs as drug carriers. a) The schematic shows FU loading on [Au₂₅(C₉-CMT)₁₈]⁻ NCs via cross-photocycloaddition reaction. Large area b) TEM and c) STEM images captured from the self-assembled NC-FU spheres. Zoom-in and focused TEM and STEM images of a single sphere are shown in (d,e). f) Elemental mapping shows the presence of gold, sulfur, fluorine, and nitrogen. g–i) 3D reconstruction electron tomogram of NC-FU assembly in different orientations and its cross-sectional view showing disc-like structure with densely packed NCs.

entities within 75 min of illumination (Figure S34b, Supporting Information). The unloading of 5-FU (under 254 nm light) from the assembled superstructures was further investigated using reverse-phase high-performance liquid chromatography (RP-HPLC). For this, a solution of purified NC-FU conjugate fabricated in THF (under 365 nm) was further illuminated under 254 nm light (75 min). Subsequently, THF was evaporated and the remaining solid was washed with HPLC mobile phase (phosphate buffer (pH 7)-methanol mixture; 97:3 in volume). During this process, disassembled NCs were precipitated, and the unloaded drug molecules were collected in

the diluent. HPLC data acquired from this diluent is in good agreement with that of the control experiment (Figure S35, Supporting Information). This clearly suggests that the 5-FU is unloaded from NC-FU conjugate in its intrinsic form. The possible physisorption of 5-FU on the NC surface was ruled out by recording and analyzing UV–vis absorption spectra from a mixture of NC and 5-FU stored in dark (Figure S36A, Supporting Information). The optical absorption features of coumarin (320 nm) and NCs (440 and 680 nm) were not changed during the incubation. The clean absorption features of NCs after precipitation and washing suggested the least

possible physisorption (Figure S36B, Supporting Information). The overall data suggests the presence of bound 5-FU on the surface of NCs during the assembly and the successful release of the drugs during the course of disassembly. Although UV light is not ideal for biological experiments, the data presented above suggest that with appropriate modifications, $[\text{Au}_{25}(\text{C}_9\text{-CMT})_{18}]^-$ NCs could be used as a noninvasive smart drug carrier in the future.

3. Conclusion

The reversible assembly of nanoparticles using a variety of stimuli is a continuously evolving area of research. Recently, light has been used as a stimulus to trigger the assembly of ligand-protected plasmonic nanoparticles and atomically precise nanoclusters. Beyond classical non-covalent interaction-driven assemblies, triggering higher-order structure formation using dynamic covalent chemistry offer possibilities to generate unprecedented nanostructures. Here, we have investigated the reversible [2+2] photocycloaddition reaction-assisted self-assembly of thiolated-coumarin protected atomically precise Au_{25} NCs. More importantly, the photocycloaddition reactions also allowed dynamic covalent chemistry at colloidal length scales. Photoactivation of NCs dispersed in THF resulted in the formation of uniform toroids. Multiple spectroscopic and microscopic techniques have been used to investigate the assembly and morphology of toroids. HR-TEM, ET reconstruction, AFM, and FESEM measurements disclosed the existence of densely packed NCs in toroids. The mechanism of toroidal formation and the role of long-term lighting on the structural reorganization of toroids have been studied in detail. The evolution of toroids has been monitored using FESEM and AFM measurements. The detailed examination revealed the formation of assembled spheres in the beginning stage of the photocycloaddition reaction. Successive lighting produced toroids by fusing the spherical intermediates. The sustained illumination of NCs finally resulted in well-organized honeycomb frameworks due to the inter-toroidal coupling. Finally, a “model-smart drug delivery system” based on the cross-photocycloaddition reaction between coumarin-tethered NC and 5-FU has been developed. The fabricated NC-based molecular carriers showed systematic loading and unloading of drugs while NCs participated in the light-induced assembly and disassembly. These “NC-based photosensitive drug delivery systems” with suitable modifications can be extended to explore noninvasive drug delivery, bioimaging, and therapeutics in the future. The assembled superstructures will be also an ideal probe for optical and electrochemical sensors.

4. Experimental Section

Reagents and Materials: In this work, analytical grade chemicals and solvents were purchased and used without further purification. Gold(III) chloride trihydrate ($\text{HAuCl}_4 \cdot 3\text{H}_2\text{O}$), tetraoctylammonium bromide (TOAB), 2-phenylethanethiol (PET), sodium borohydride (NaBH_4), potassium thioacetate (KSCoCH_3), *trans*-2-3-(4-*tert*-butylphenyl)-2-methyl-2-propenylidenemalononitrile (DCTB), acetone, methanol, hydrochloric acid (HCl), tetrahydrofuran (THF), *N*, *N*'-

dimethyl formamide (DMF), dichloromethane (DCM), and toluene were purchased from Sigma-Aldrich. 7-hydroxycoumarin, 1,3-dibromopropane, and 1,9-dibromononane were purchased from Tokyo Chemicals Industry (TCI). 5-Fluorouracil was purchased from Alfa Aesar. Potassium carbonate (K_2CO_3), potassium iodide (KI), anhydrous sodium sulfate (Na_2SO_4), Chloroform-*d* (CDCl_3), and tetrahydrofuran-*d* ($\text{THF-}d_8$) were purchased from Sisco Research Laboratories (SRL).

Instrumentation and Characterization: The nuclear magnetic resonance (NMR) spectroscopy (^1H and ^{13}C) analysis was performed using Bruker AVANCE III HD 400 MHz spectrometers. VARIAN Cary 500 Scan spectrometer was used to measure the absorbance spectra (UV–vis) of ligands, NCs, and superstructures. The Bruker Tensor 27 spectrometer was used for FT-IR spectra (attenuated total reflection). The Orbitrap Elite Hybrid Ion Trap-Orbitrap (Thermo Fisher Scientific) mass spectrometer was used for measuring high-resolution mass spectrometry (HR-MS). The mass spectrum of NC was recorded using Bruker Microflex matrix-assisted laser desorption ionization time-of-flight (MALDI-TOF) mass spectrometry. The ionization of molecules was achieved using Nd:YAG laser ($\lambda = 266$ nm). A standard solution of the matrix was prepared by dissolving 10 mg DCTB in 500 μL DCM. NC solution was prepared at a ratio of 1 mg in 100 μL DCM. Different compositions of matrix and NC solution were tried to optimize the well-resolved spectrum. High-resolution transmission electron microscopy (HR-TEM) and STEM images with energy dispersive X-ray spectroscopy (EDS) and elemental maps were recorded from FEI Talos F200S (200 kV) transmission electron microscope. Jeol F200 S/TEM electron microscope operated at 200 keV was used for collecting data for 3D electron tomographic reconstruction. For tomographic reconstruction, 2D projections were collected between $\pm 69^\circ$ with increment angles of 2° . The acquired raw 2D projections were first subjected to a series of preprocessing using the IMOD software package.^[24] Coarse alignment was used to create the aligned file. A custom-made maximum entropy method (MEM) program was used for 3D reconstruction.^[25] Chimera was used to produce colored images. Agilent Technologies 5500 series AFM/SPM microscope with Pico View 1.14.1. software and WSxM 5.0 was used to measure AFM images. Carl-Zeiss SUPRA 55VP field emission scanning electron microscope was used for FESEM images with EDS and elemental mapping. Thermo Scientific ESCALAB 250Xi instrument was used to measure X-ray photoelectron spectra. The photodimerization of chromophore and NC were performed using a Spectroline E-Series UV lamp (102 lx for 365 nm and 70 lx for 254 nm). The SHIMADZU LC-20AD model system linked to the LC solution software was used for HPLC analysis. A reverse-phase column, CLC-ODS-C18 (250 \times 4.6 mm, 5 μm) has been used as the stationary phase. The detection was completed by isocratic elution of the mobile phase at the detection wavelength of 267 nm (at ambient temperature with an injection volume and flow rate of 20 μL and 1.0 mL min^{-1}). DLS measurements were performed in Zetasizer Nano S90 (Malvern). The DFT has been used to procure the energy-minimized structure of NC.^[26–28]

Synthesis of Molecule 1 (M1): M1 was synthesized using a reported protocol.^[14a] A mixture of 7-hydroxycoumarin (1.3 g, 8 mmol), 1,9-dibromononane (16.3 mL, 80 mmol), K_2CO_3 (1.33 g, 9.6 mmol), and a catalytic amount of KI was heated in acetone (100 mL) at 80 $^\circ\text{C}$ for 4 h. The temperature of the reaction mixture was reduced to RT, the solid was filtered out, and the solvent was evaporated off. The crude filtrate was column chromatographed over silica gel, using hexane as eluent to remove the excess 1,9-dibromononane, followed by 10% ethyl acetate/hexane to afford M1 (solid; melting point: 45 $^\circ\text{C}$; 2.85 g; 96% yield). ^1H NMR (400 MHz, CDCl_3); $\delta = 7.63$ (d, $J = 9.5$ Hz, 1H), 7.36 (d, $J = 8.5$ Hz, 1H), 6.86 – 6.77 (m, 2H), 6.24 (d, $J = 9.4$ Hz, 1H), 4.00 (t, $J = 6.5$ Hz, 2H), 3.41 (t, $J = 6.8$ Hz, 2H), 1.90 – 1.76 (m, 4H), and 1.51 – 1.31 (m, 10H); ^{13}C NMR (100 MHz, CDCl_3); $\delta = 162.50, 161.42, 156.01, 143.60, 128.82, 113.09, 113.00, 112.47, 101.40, 68.70, 34.16, 32.88, 29.42, 29.30, 29.04, 28.77, 28.22, \text{ and } 26.01$; FT-IR (ν_{max}) = 2930, 2852, 1728, 1612, 1290, 1233, 1127, 839, 740, and 627 cm^{-1} . HR-MS ($\text{C}_{18}\text{H}_{23}\text{O}_3\text{Br}$), $m/z + 1 = 367.08$ and 369.09. ^1H and ^{13}C NMR, FT-IR, and HR-MS spectra of M1 are shown in Figures S1–S3, Supporting Information.

Synthesis of Molecule 2 (M2): M2 was synthesized by adopting a reported protocol with required modifications.^[29] A solution of M1 (2.83 g, 7.7 mmol) and KSCoCH_3 (1.06 g, 9.24 mmol) in acetone

(120 mL) was stirred overnight at RT. After the reaction, the mixture was filtered and concentrated. The crude was extracted with ethyl acetate (3 × 20 mL) and the organic layer was evaporated under a vacuum. The crude mixture was purified by a silica column using 15% ethyl acetate/hexane to yield M2 (solid; melting point: 68 °C; 2.5 g; 89% yield). ¹H NMR (400 MHz, CDCl₃); δ = 7.62 (d, *J* = 9.4 Hz, 1H), 7.35 (d, *J* = 8.6 Hz, 1H), 6.85 – 6.76 (m, 2H), 6.22 (d, *J* = 9.5 Hz, 1H), 3.99 (t, *J* = 6.5 Hz, 2H), 2.85 (t, *J* = 7.3 Hz, 2H), 2.31 (s, 3H), 1.79 (p, *J* = 6.7 Hz, 2H), and 1.6 – 1.27 (m, 12H); ¹³C NMR (100 MHz, CDCl₃); δ = 195.09, 161.38, 160.30, 154.88, 142.47, 127.68, 111.97, 111.86, 111.33, 100.27, 67.59, 29.64, 28.45, 28.31, 28.20, 28.09, 27.98, 27.91, 27.73, and 24.88; FT-IR (*v*_{max}) = 2924, 2852, 1730–1690, 1618, 1285, 1237, 1131, 829, and 714 cm⁻¹. HR-MS (C₂₀H₂₆O₄S), *m/z* + 1 = 363.16. ¹H and ¹³C NMR, FT-IR, and HR-MS spectra of M2 are shown in Figures S4–S6, Supporting Information.

Synthesis of Molecule 3 (M3): M3 was synthesized following the reported protocol with required modifications.^[29] M2 (1.3 g, 3.6 mmol) was hydrolyzed in 1.25 M HCl/methanol mixture (50 mL) for 2 h at 65 °C. The reaction mixture was evaporated to remove the solvent, extracted with ethyl acetate (2 × 50 mL), dried over anhydrous Na₂SO₄, and concentrated. The mixture was purified by a silica column using 10% ethyl acetate/hexane to afford M3 (solid; melting point: 41 °C; 0.83 g; 72% yield). ¹H NMR (400 MHz, CDCl₃); δ = 7.62 (d, *J* = 9.5 Hz, 1H), 7.36 (s, 1H), 6.86 – 6.76 (m, 2H), 6.23 (d, *J* = 9.5 Hz, 1H), 3.99 (t, *J* = 6.5 Hz, 2H), 2.51 (q, *J* = 7.4 Hz, 2H), 1.79 (p, *J* = 6.7 Hz, 2H), 1.60 (p, *J* = 7.2 Hz, 2H), and 1.51 – 1.25 (m, 11H); ¹³C NMR (100 MHz, CDCl₃); δ = 162.50, 161.43, 156.00, 143.60, 128.81, 113.09, 112.98, 112.45, 101.38, 68.71, 34.09, 29.48, 29.34, 29.07, 29.04, 28.41, 26.02, and 24.74; FT-IR (*v*_{max}) = 2929, 2853, 2543, 1730, 1615, 1289, 1234, 1129, 842, and 722 cm⁻¹. HR-MS (C₁₈H₂₄O₃S), *m/z* + 1 = 321.15. ¹H and ¹³C NMR, FT-IR, and HR-MS spectra of M3 are shown in Figures S7–S9, Supporting Information. This molecule was called C₉-CMT.

Synthesis of Molecule 4 (M4): M4 was synthesized by following a known protocol with required changes.^[14a] A mixture of 7-hydroxycoumarin (1.3 g, 8 mmol), 1,3-dibromopropane (8.18 mL, 80 mmol), K₂CO₃ (1.32 g, 9.62 mmol), and a catalytic amount of KI was heated in acetone (100 mL) at 80 °C for 4 h. The reaction mixture was cooled, filtered, and evaporated to pump out the solvent. The crude filtrate was column chromatographed over silica gel, using hexane as eluent to remove the excess 1,3-dibromopropane, followed by 10% ethyl acetate/hexane to afford M4 (solid; melting point: 96 °C; 2.1 g; 93% yield). ¹H NMR (400 MHz, CDCl₃); δ = 7.63 (d, *J* = 9.5 Hz, 1H), 7.37 (d, *J* = 8.4 Hz, 1H), 6.87 – 6.80 (m, 2H), 6.25 (d, *J* = 9.5 Hz, 1H), 4.17 (t, *J* = 5.8 Hz, 2H), 3.61 (t, *J* = 6.4 Hz, 2H), and 2.35 (p, *J* = 6.1 Hz, 2H); ¹³C NMR (100 MHz, CDCl₃); δ = 161.96, 161.27, 155.94, 143.50, 128.95, 113.37, 112.86, 112.84, 101.65, 65.97, 32.06, and 29.69. FT-IR (*v*_{max}) = 2923, 2850, 1712, 1616, 1284, 1227, 1130, 833, 740, and 633 cm⁻¹. ¹H and ¹³C NMR and FT-IR spectra of M4 are shown in Figures S10 and S11, Supporting Information.

Synthesis of Molecule 5 (M5): M5 was synthesized using a reported procedure with necessary modifications.^[29] A solution of M4 (2 g, 7 mmol) and KSCoCH₃ (0.97 g, 8.5 mmol) in acetone (110 mL) was stirred overnight at RT. After the reaction, the mixture was filtered and concentrated. The crude filtrate was purified by a silica column using 15% ethyl acetate/hexane to yield M5 (solid; melting point: 62 °C; 1.7 g; 87% yield). ¹H NMR (400 MHz, CDCl₃); δ = 7.63 (d, *J* = 9.5 Hz, 1H), 7.36 (d, *J* = 8.6 Hz, 1H), 6.90 – 6.74 (m, 2H), 6.24 (d, *J* = 9.4 Hz, 1H), 4.05 (t, *J* = 6.1 Hz, 2H), 3.05 (t, *J* = 7.1 Hz, 2H), 2.34 (s, 3H), and 2.09 (p, *J* = 6.6 Hz, 2H); ¹³C NMR (100 MHz, CDCl₃); δ = 195.77, 162.08, 161.34, 155.94, 143.54, 128.90, 113.24, 113.01, 112.72, 101.48, 66.85, 30.77, 29.12, and 25.79. FT-IR (*v*_{max}) = 2923, 2857, 1700–1683, 1611, 1289, 1232, 1124, 817, and 720 cm⁻¹. ¹H and ¹³C NMR and FT-IR spectra of M5 are shown in Figures S12 and S13, Supporting Information.

Synthesis of Molecule 6 (M6): M6 was synthesized using a reported protocol with required modifications.^[29] M5 (1 g, 3.6 mmol) was hydrolyzed in 1.25 M HCl/methanol mixture (50 mL) for 2 h at 65 °C. The reaction mixture was rotary evaporated to remove solvent and extracted with ethyl acetate (2 × 50 mL), dried using anhydrous Na₂SO₄, and concentrated. The crude mixture was purified by a silica column using 10% ethyl acetate/hexane to yield M6 (solid; melting point: 72 °C; 0.61 g;

72% yield). ¹H NMR (400 MHz, CDCl₃); δ = 7.63 (d, *J* = 9.5 Hz, 1H), 7.36 (d, *J* = 8.4 Hz, 1H), 6.87 – 6.78 (m, 2H), 6.24 (d, *J* = 9.4 Hz, 1H), 4.14 (t, *J* = 5.9 Hz, 2H), 2.74 (q, *J* = 7.4 Hz, 2H), 2.11 (p, *J* = 6.4 Hz, 2H), and 1.40 (t, *J* = 8.1 Hz, 1H); ¹³C NMR (100 MHz, CDCl₃); δ = 162.14, 161.34, 155.96, 143.54, 128.91, 113.25, 112.95, 112.72, 101.54, 66.31, 33.06, and 21.19. FT-IR (*v*_{max}) = 2928, 2865, 2574, 1724, 1610, 1288, 1232, 1124, 843, and 740 cm⁻¹. ¹H and ¹³C NMR and FT-IR spectra of M6 are shown in Figures S14 and S15, Supporting Information. This molecule was called C₃-CMT.

Synthesis of [Au₂₅(PET)₁₈]⁻ NCs: [Au₂₅(PET)₁₈]⁻ NCs were synthesized using a reported procedure.^[16,14a]

Synthesis of [Au₂₅(C₉-CMT)₁₈]⁻ NCs: The synthesis of [Au₂₅(C₉-CMT)₁₈]⁻ NCs was performed using the reported method in the literature.^[16,14a] In a typical synthesis, TOAB (33 mg in 1.75 mL THF) was injected into a HAuCl₄·3H₂O (20 mg in 2 mL THF) and stirred at 25 °C until the color of the mixed solution changed to dark red. Subsequently, 81 mg of C₉-CMT was directly added and the resulting solution was stirred for another 1 h. The reduction of Au-thiolate was performed by injecting 1.25 mL of freshly made ice-cold aqueous NaBH₄ (19 mg) solution. In order to complete the formation of Au₂₅ NCs, the above mixture was stirred at RT for an extra 4–5 h. The organic and aqueous layers were separated using a separatory funnel. The addition of 1 mL of toluene helped to separate the immiscible layers clearly. The separated organic portion was washed many times with DI water and subsequently pumped out using a rotary evaporator. The unreacted thiols and other unwanted products were separated by precipitating the NCs using methanol (10 mL). The supernatant solution containing the free thiol was discarded. This washing step was continued two to three times. Finally, the dried [Au₂₅(C₉-CMT)₁₈]⁻ NCs were stored in a refrigerator and have been used for further characterization.

Supporting Information

Supporting Information is available from the Wiley Online Library or from the author.

Acknowledgements

E.S.S. thanks Science and Engineering Research Board (SERB) for Ramanujan Fellowship (SB/S2/RJN-005/2017) and Startup Research grant (SRG/2022/586). The authors thank DST-UNS (DST Unit of Nanoscience) and TUE (Thematic Unit of Excellence) of IIT Madras for HRTEM and DFT support. The authors thank the CIF (Central Instrumentation Facility) of CSIR-CECRI for the instrumentation support. Prof. T. Pradeep (IIT Madras), Prof. Vijayamohan K. Pillai (IISER Tirupati; former Director CSIR-CECRI, Karaikudi), Dr. N. Kalaiselvi (DG-CSIR, former Director CSIR-CECRI, Karaikudi), Prof. M. K. Jayaraj (Vice-Chancellor, University of Calicut), Prof. S. Sampath (IISc Bangalore), Prof. M. M. Shajumon (IISER Thiruvananthapuram), Dr. Jatish Kumar (IISER Tirupati), Dr. S. Sathiyarayanan (Former Head, PPMG, CSIR-CECRI), Dr. Sreekuttan Unni (CSIR-CECRI, Madras Unit, Chennai), Miss. P. Mymoona (CSIR-CECRI, Karaikudi), Dr. K. Fazalurahman (University of Calicut), Dr. Reji Thomas (Farook College Calicut), Mr. K. T. Ibrahim (University of Calicut), and Mr. M. Arjun (University of Calicut) are acknowledged for their support. CSIR-CECRI manuscript communication number is CECRI/PESVC/Pubs/2022-137. The authors thank the Academy of Finland for project funding (BioBase, Decision no: 352900), Photonic Research and Innovation (PREIN) flagship, Tampere Microscopy Center for microscopy facilities, and Dr. Mari Honkanen, Tampere University, Finland for technical support.

Conflict of Interest

The authors declare no conflict of interest.

Author Contributions

K.M.L. and J.V.R. contributed equally to this work. The project was conceived by E.S.S. The chromophores and nanoclusters were synthesized by K.M.L. and R.J. All experiments were performed by K.M.L., R.J., and E.S.S. Electron tomography data acquisition and reconstruction were performed by N.

Data Availability Statement

The data that support the findings of this study are available in the supplementary material of this article.

Keywords

5-fluorouracil, coumarin, drug loading, dynamic covalent chemistry, photocycloaddition, precision nanoclusters, self-assembly, toroidal superstructures

Received: November 16, 2022

Revised: January 4, 2023

Published online: January 22, 2023

- [1] a) G. M. Whitesides, B. Grzybowski, *Science* **2002**, 295, 2418; b) M. Grzelczak, J. Vermant, E. M. Furst, L. M. Liz-Marzán, *ACS Nano* **2010**, 4, 3591; c) B. L. V. Prasad, C. M. Sorensen, K. J. Klabunde, *Chem. Soc. Rev.* **2008**, 37, 1871; d) S. Wang, H. Yao, S. Sato, K. Kimura, *J. Am. Chem. Soc.* **2004**, 126, 7438; e) K. J. M. Bishop, C. E. Wilmer, S. Soh, B. A. Grzybowski, *Small* **2009**, 5, 1600; f) R. Klajn, J. F. Stoddart, B. A. Grzybowski, *Chem. Soc. Rev.* **2010**, 39, 2203; g) W. Cheng, M. J. Campolongo, J. J. Cha, S. J. Tan, C. C. Umbach, D. A. Muller, D. Luo, *Nat. Mater.* **2009**, 8, 519.
- [2] a) D. Manna, T. Udayabhaskararao, H. Zhao, R. Klajn, *Angew. Chem., Int. Ed.* **2015**, 54, 12394; b) R. Klajn, K. J. M. Bishop, B. A. Grzybowski, *Proc. Natl. Acad. Sci. U. S. A.* **2007**, 104, 10305.
- [3] a) M.-C. Daniel, D. Astruc, *Chem. Rev.* **2004**, 104, 293; b) C. J. Murphy, T. K. Sau, A. M. Gole, C. J. Orendorff, J. Gao, L. Gou, S. E. Hunyadi, T. Li, *J. Phys. Chem. B* **2005**, 109, 13857; c) Z. Nie, A. Petukhova, E. Kumacheva, *Nat. Nanotechnol.* **2010**, 5, 15; d) A. Chakraborty, Nonappa, B. Mondal, K. Chaudhari, H. Rekola, V. Hynninen, M. A. Kostianen, R. H. A. Ras, T. Pradeep, *J. Phys. Chem. C* **2021**, 125, 3256; e) M. Frascioni, R. Tel-Vered, M. Riskin, I. Willner, *Anal. Chem.* **2010**, 82, 2512; f) M. Hentschel, M. Schäferling, X. Duan, H. Giessen, N. Liu, *Sci. Adv.* **2017**, 3, e1602735.
- [4] a) Nonappa, T. Lahtinen, J. S. Haataja, T.-R. Tero, H. Häkkinen, O. Ikkala, *Angew. Chem., Int. Ed.* **2016**, 55, 16035; b) Nonappa, J. S. Haataja, J. V. I. Timonen, S. Malola, P. Engelhardt, N. Houbenov, M. Lahtinen, H. Häkkinen, O. Ikkala, *Angew. Chem., Int. Ed.* **2017**, 56, 6473.
- [5] a) G. Schmid, *Chem. Rev.* **1992**, 92, 1709; b) R. L. Whetten, J. T. Khoury, M. M. Alvarez, S. Murthy, I. Vezmar, Z. L. Wang, P. W. Stephens, C. L. Cleveland, W. D. Luedtke, U. Landman, *Adv. Mater.* **1996**, 8, 428; c) Y. Negishi, K. Nobusada, T. Tsukuda, *J. Am. Chem. Soc.* **2005**, 127, 5261; d) H. Häkkinen, *Chem. Soc. Rev.* **2008**, 37, 1847; e) J. F. Parker, C. A. Fields-Zinna, R. W. Murray, *Acc. Chem. Res.* **2010**, 43, 1289; f) S. Yamazoe, K. Koyasu, T. Tsukuda, *Acc. Chem. Res.* **2014**, 47, 816; g) R. Jin, *Nanoscale* **2015**, 7, 1549; h) R. Jin, C. Zeng, M. Zhou, Y. Chen, *Chem. Rev.* **2016**, 116, 10346; i) I. Chakraborty, T. Pradeep, *Chem. Rev.* **2017**, 117, 8208; j) Q. Yao, T. Chen, X. Yuan, J. Xie, *Acc. Chem. Res.* **2018**, 51, 1338; k) P. Chakraborty, A. Nag, A. Chakraborty, T. Pradeep, *Acc. Chem. Res.* **2019**, 52, 2.
- [6] a) J. V. Rival, P. Mymoona, K. M. Lakshmi, Nonappa, T. Pradeep, E. S. Shibu, *Small* **2021**, 17, 2005718; b) Z. Wu, Q. Yao, S. Zang, J. Xie, *ACS Mater. Lett.* **2019**, 1, 237; c) Q. Yao, Z. Wu, Z. Liu, Y. Lin, X. Yuan, J. Xie, *Chem. Sci.* **2021**, 12, 99; d) E. Banach, T. Bürgi, *Helv. Chim. Acta* **2022**, 105, 202100186.
- [7] Nonappa, O. Ikkala, *Adv. Funct. Mater.* **2018**, 28, 1704328.
- [8] S. Chandra, Nonappa, G. Beaune, A. Som, S. Zhou, J. Lahtinen, H. Jiang, J. V. I. Timonen, O. Ikkala, R. H. A. Ras, *Adv. Opt. Mater.* **2019**, 7, 1900620.
- [9] A. Som, A. Griffo, I. Chakraborty, H. Hähl, B. Mondal, A. Chakraborty, K. Jacobs, P. Laaksonen, O. Ikkala, T. Pradeep, Nonappa, *Small* **2022**, 18, 2201707.
- [10] a) R. Huang, Y. Wei, X. Dong, X. Wu, C. Du, *Nat. Chem.* **2017**, 9, 689; b) S. Basu, A. Paul, A. Chattopadhyay, *J. Mater. Chem. A* **2016**, 4, 1218.
- [11] a) Z. Wu, Y. Li, J. Liu, Z. Lu, H. Zhang, B. Yang, *Angew. Chem., Int. Ed.* **2014**, 53, 12196; b) M. Cao, R. Pang, Q.-Y. Wang, Z. Han, Z.-Y. Wang, X.-Y. Dong, S.-F. Li, S.-Q. Zang, T. C. W. Mak, *J. Am. Chem. Soc.* **2019**, 141, 14505.
- [12] Z. Wu, J. Liu, Y. Gao, H. Liu, T. Li, H. Zou, Z. Wang, K. Zhang, Y. Wang, H. Zhang, B. Yang, *J. Am. Chem. Soc.* **2015**, 137, 12906.
- [13] M. Wang, Y. Chen, W. Cai, H. Feng, T. Du, W. Liu, H. Jiang, A. Pasquarelli, Y. Weizmann, X. Wang, *Proc. Natl. Acad. Sci. U. S. A.* **2020**, 117, 308.
- [14] a) J. V. Rival, Nonappa, E. S. Shibu, *ACS Appl. Mater. Interfaces* **2020**, 12, 14569; b) T. Udayabhaskararao, P. K. Kundu, J. Ahrens, R. Klajn, *Chemphyschem* **2016**, 17, 1805.
- [15] a) H. He, M. Feng, Q. Chen, X. Zhang, H. Zhan, *Angew. Chem., Int. Ed.* **2016**, 55, 936; b) Y. Chen, Z. Wang, Y. He, Y. J. Yoon, J. Jung, G. Zhang, Z. Lin, *Proc. Natl. Acad. Sci. U. S. A.* **2018**, 115, E1391.
- [16] M. Zhu, E. Lanni, N. Garg, M. E. Bier, R. Jin, *J. Am. Chem. Soc.* **2008**, 130, 1138.
- [17] a) A. Dass, A. Stevenson, G. R. Dubay, J. B. Tracy, R. W. Murray, *J. Am. Chem. Soc.* **2008**, 130, 5940; b) K. Salorinne, S. Malola, O. A. Wong, C. D. Rithner, X. Chen, C. J. Ackerson, H. Häkkinen, *Nat. Commun.* **2016**, 7, 10401.
- [18] G. Li, C. Liu, Y. Lei, R. Jin, *Chem. Commun.* **2012**, 48, 12005.
- [19] a) N. K. Mal, M. Fujiwara, Y. Tanaka, *Nature* **2003**, 421, 350; b) A. Concellón, T. Liang, A. P. H. J. Schenning, J. L. Serrano, P. Romero, M. Marcos, *J. Mater. Chem. C* **2018**, 6, 1000; c) Y. Chen, R.-T. Hong, *J. Polym. Res.* **1994**, 1, 285.
- [20] H. Huang, B. Chung, J. Jung, H.-W. Park, T. Chang, *Angew. Chem., Int. Ed.* **2009**, 48, 4594.
- [21] a) D. Li, X. Jia, X. Cao, T. Xu, H. Li, H. Qian, L. Wu, *Macromolecules* **2015**, 48, 4104; b) K. Zhang, H. Miao, D. Chen, *J. Am. Chem. Soc.* **2014**, 136, 15933.
- [22] a) Z. Jia, V. A. Bobrin, M. J. Monteiro, *ACS Macro Lett.* **2017**, 6, 1223; b) R. Deng, F. Liang, W. Li, S. Liu, R. Liang, M. Cai, Z. Yang, J. Zhu, *Small* **2013**, 9, 4099.
- [23] P. Xu, L. Gao, C. Cai, J. Lin, L. Wang, X. Tian, *Adv. Funct. Mater.* **2022**, 32, 2106036.
- [24] J. R. Kremer, D. N. Mastrorarde, J. R. McIntosh, *J. Struct. Biol.* **1996**, 116, 71.
- [25] a) P. Engelhardt, in *Electron Microscopy*, (Ed: J. Kuo), Humana Press, Totowa, NJ **2007**, p. 365; b) P. Engelhardt, in *Encyclopedia of Analytical Chemistry*, (Ed: R.A. Meyers), John Wiley & Sons Ltd, Chichester, UK **2006**, p. 4948.
- [26] a) J. Enkovaara, C. Rostgaard, J. J. Mortensen, J. Chen, M. Duřák, L. Ferrighi, J. Gavnholt, C. Glinsvad, V. Haikola, H. A. Hansen, H. H. Kristoffersen, M. Kuisma, A. H. Larsen, L. Lehtovaara, M. Ljungberg, O. Lopez-Acevedo, P. G. Moses, J. Ojanen, T. Olsen,

- V. Petzold, N. A. Romero, J. Stausholm-Møller, M. Strange, G. A. Tritsarlis, M. Vanin, M. Walter, B. Hammer, H. Häkkinen, G. K. H. Madsen, R. M. Nieminen, et al., *J. Phys.: Condens. Matter* **2010**, *22*, 253202; b) J. J. Mortensen, L. B. Hansen, K. W. Jacobsen, *Phys. Rev. B* **2005**, *71*, 035109.
- [27] J. P. Perdew, K. Burke, M. Ernzerhof, *Phys. Rev. Lett.* **1996**, *77*, 3865.
- [28] W. Humphrey, A. Dalke, K. Schulten, *J. Mol. Graphics* **1996**, *14*, 33.
- [29] T.-C. Zheng, M. Burkart, D. E. Richardson, *Tetrahedron Lett.* **1999**, *40*, 603.